Effect of N_2 and CO_2 bubbles on gas volume fraction and flow pattern in a quasi-2D bubble column by shadow imaging

Sarker, D.; Schinkel, C. V.; Portela, L. M.

DOI
10.1016/j.cherd.2022.11.032

Publication date
2023

Document Version
Final published version

Published in
Chemical Engineering Research and Design

Available online at www.sciencedirect.com

Chemical Engineering Research and Design

journal homepage: www.elsevier.com/locate/cherd

Effect of N_2 and CO_2 bubbles on gas volume fraction and flow pattern in a quasi-2D bubble column by shadow imaging

D. Sarker[a,b,*], C.V. Schinkel[a], L.M. Portela[a]

[a] Section of Transport Phenomena, Department of Chemical Engineering, Delft University of Technology, 2629Hz Delft, the Netherlands

[b] Department of Mechanical Engineering, International University of Business Agriculture and Technology, Dhaka 1230, Bangladesh

ARTICLE INFO

Article history:
Received 8 September 2022
Received in revised form
3 November 2022
Accepted 21 November 2022
Available online 25 November 2022

Keywords:
Visual imaging
Bubbly flow
CO_2 bubble-bubble interaction
Light intensity
Power spectral density
Cross-correlation

ABSTRACT

This study reports the effect of N_2 and CO_2 bubbles on dilute to dense gas-liquid two-phase bubbly flow. A shadowgraph imaging technique captured bubble images at a high spatiotemporal resolution. The recordings of bubble images allow us to compute gas fraction distribution. It requires challenging segmentation and gas-liquid interface detection approaches in image processing. Hence a novel gas contour characterization technique has been introduced in this study that analyses light intensity per pixel for quantifying the effect of local gas volume fraction. The dominant gas structure and repetitive gas pattern have also been determined here using Fourier transform-based power spectral density and 2D cross-correlation functions, respectively. Gas-liquid flow regimes of dissolved CO_2 bubbles are found quite different than that of N_2 bubbles. The plausible reasons are that gas fraction distribution at the sparger region may inhibit bubble coalescence and the positive surface charge of CO_2 bubbles acts as a barrier to the interface deformation.

1. Introduction

Two-phase bubbly flow is frequently encountered in a wide range of industrial applications such as crude oil production, separation through membrane contactors, refining techniques, wastewater treatment, fermentation, etc. It can be simply generated in lab-scale by injecting gas bubbles into the bulk liquid of a bubble column reactor (BCR). BCR is extensively used as multiphase contactors to carry out the chemical reaction processes. Efficiency of BCR is influenced by bubble-induced liquid mixing and gas-liquid mass transfer. A lack of well-designed experiment causes a scarce knowledge of conjugate effect of mass transfer and hydrodynamics on dense bubbly flow. Comparing the dynamics of gas volume fraction (GVF) distribution of dissolving (CO_2) and non-dissolving (N_2) bubbles could be one of the ways to investigate this aspect. The differences in mass solubility of N_2 and CO_2 bubbles and their impact on bubble-bubble interactions will possibly result a clear distinction between their flow regimes.

1.1. *Bubbly flow and its influential parameter*

1.1.1. *Influential parameters*

The key parameters to design and scale up of BCR are GVF distribution and liquid circulation velocity (Heijnen and Van'T Riet, 1984; Panicker, 2017). Gas holdup is dependent on various parameters such as superficial gas velocity, pressure, temperature, column dimensions, gas distributor design, and solid phase properties (Kantarci et al., 2005). The common consensus is that superficial gas velocity (U_g) is positively correlated with GVF in homogeneous bubbly flow and not

* Corresponding author at: Section of Transport Phenomena, Department of Chemical Engineering, Delft University of Technology, 2629Hz Delft, the Netherlands.
E-mail address: dsarker.me@iubat.edu (D. Sarker).

https://doi.org/10.1016/j.cherd.2022.11.032

correlated with small GVFin highly heterogeneous regime. The effect of column aspect ratio (AR) on flow regime transition is profound for $AR < 3$ (Besagni et al., 2018a) and can be neglected for $AR > 3$ (Laupsien, 2017). Fine needle spargers (inner diameter < 1 mm) result uniform distribution of bubble size at sparger and eventually stabilize homogeneous flow regime (Mudde et al., 2009). The influence of gas sparger diminishes in heterogeneous regime (Besagni et al., 2018b). The size of bubble increases with liquid surface tension and viscosity (Schaefer et al., 2002). An increase of gas density (ρ_g) decreases bubble size, increases bubble break-up, and increases GVF (Schaefer et al., 2002; Wilkinson and L.L.L., 1990). ρ_g also affects bubble formation, void fraction, bubble breakup, and flow regime transition (Wilkinson and L.L.L., 1990; Krishna and L. L, 1991; Hecht et al., 2015). For instance, 2 times increase of GVF was reported due to increase of ρ_g from 1 to 10 kg/m^3 at U_g= 0.12 m/s (Krishna and L. L, 1991). Additionally, influence of ρ_g (> 2 kg/m^3) on the bubble breakup is significant as well for large bubbles (~10 mm) (Wilkinson and L.L.L., 1990).

1.1.2. *Flow regime*

In a bubbly flow, gas bubbles rise upward from the sparger with small scale transverse and axial oscillations through a continuous liquid phase. Despite of uniformity in GVF in the homogeneous regime, bubbles have a natural tendency to form cluster due to the hydrodynamic interactions (Risso, 2018). With the increase of U_g, bubbles agglomerate and form a large gas fraction. As a result, the flow regime becomes heterogeneous (Ruzicka et al., 2001). Due to bubble-liquid interactions, some of the large gas fractions break up and produce a number of small bubbles. The large gas fractions travels upward with oscillations through the center of BCR and induce macroscale liquid circulations (Mudde, 2005; Zahradník et al., 1997) on the side of BCR wherein small bubbles are trapped. The oscillations of large gas fractions become weaker as they reach the upper part of BCR (Darmana et al., 2007). Thus, a wide distribution of gas fractions is found in a heterogeneous bubbly flow. The bubbles may grow as they rise along the column height because of reduction of hydrostatic pressure (Hlawitschka et al., 2017). CO_2 gas flow regime attains additional features such as gas dissolution and complex mechanism of bubble interactions.

1.2. *Bubble-bubble interactions*

1.2.1. *Dissolution of CO_2 bubbles*

Gas-liquid mass transfers through a very thin diffusion layer at the front part of a bubble (Colombet et al., 2015) and at the rear side of the bubble, convection-driven mass transfer had been reported (Weiner et al., 2019). Mass transfer is influenced by bubble size, bubble velocity, and velocity fluctuations (Aboulhasanzadeh and Tryggvason, 2014; Nock et al., 2016) and gradually decreases with time (Farajzadeh et al., 2007). CO_2 bubbles induce convective mixing and enhance mass transfer (Kong, 2019). Li et al. (2019a). disagrees with this findings and concluded that bubble size is negatively correlated with the mass transfer efficiency. However, they did not consider convective transport of chemical species. Both the studies (Kong, 2019; Li et al., 2019a) nevertheless agreed that dissolving CO_2 bubbles follow the flow trajectories. Hlawitschka et al (Hlawitschka et al., 2017). supported this findings and deduced that CO_2 bubbles mostly dissolves at the upper part of a BCR. Dissolution of CO_2 bubbles is more intense in deionized water than in the contaminated water, as surfactant molecules deposit on the surface of a bubble in the contaminated water (Huang and Saito, 2015).

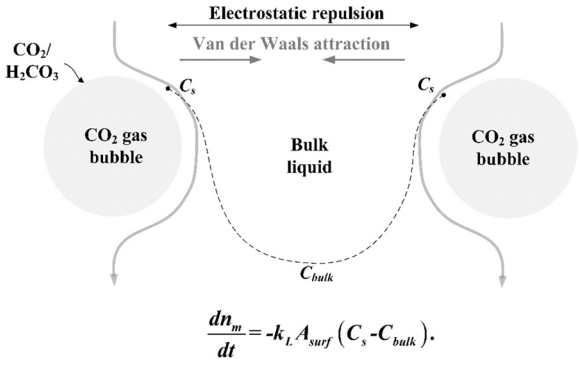

Fig. 1 – Conceptual idea of CO2 bubble-bubbleinteractions mechanism based on DLVO theory
Adopted from (Yaminsky et al., 2010; Tabor et al., 2011; Weiner and Bothe, 2017; Li et al., 2019b).

1.2.2. *Interactions of CO_2 bubbles*

Bubble-bubble interaction enhances mass transfer as it refreshes the boundary layer of bubble, whereas bubble induced liquid mixing has insignificant impact on the dissolution of bubbles (Kong, 2019). Many investigators found that BSD at the sparger plays a vital role in bubble breakup and coalescence. According to the authors best knowledge, effect of mass transfer on the interaction of CO_2 bubbles are yet to be investigated. Here we postulate a coalescence mechanism of CO_2 bubbles based on the long-range electrostatic repulsion and the short-range Van der Waals attraction (Fig. 1). The dashed line in Fig. 1 represents CO_2 concentration gradient. Dissolution of CO_2 gas bubbles in water forms CO_2(aq), bicarbonate (HCO_3^-) ions, carbonic acid (H_2CO_3), and CO_3^{2-}Harper (2007). Protons (H^+) dissociates during the reactions. Carbonaceous species is the source of surface charge and produces an electric field around bubble surface that results electrostatic repulsion. Prior to the coalescence, bubbles approach to each other at low velocities (Yaminsky et al., 2010) and the trapped film in between bubbles becomes very thin. The surface potential of N_2, air and Ar bubbles is less than zero and positive for CO_2 bubbles at pH= 4.0 – 7.0 (Tabor et al., 2011, 2012). Hence, high energy barrier of CO_2 bubbles retard thinning of the film which needs to be overcome for bubble coalescence (Katsir and Marmur, 2014). Tabor et al (Tabor et al., 2011). found that CO_2 bubbles do not coalesce below pH 6. Laupsien (Li et al., 2019a) argued in another way that the critical intervals related to bubble coalescence are larger for non-dissolving bubbles than that for dissolving bubbles and diameter of dissolving bubble is inversely correlated with the interval length. He commented that concentration of species around the dissolving bubbles influence bubble coalescence.

1.3. *Bubble size distribution*

Determination of bubble size distribution (BSD) is a common practice for characterizing bubbly flow. The widely accepted idea is that BSD in the bulk is the result of BSD at sparger region which is closely related to bubble formation process and this process is a function of U_g, sparger design, and

chamber volume (Harteveld, 2005). Recently, Lucas and Ziegenhein (Lucas and Ziegenhein, 2019) found that initial *BSD* at sparger is the critical parameter regardless of U_g for the stability of flow regime. *BSD* of homogeneous flow in a N_2 gas-aqueous solution system was manifested by a unimodal Gaussian curve (Marrucci and Nicodemo, 1967). A log-normal distribution curve of *BSD* was obtained due to fine-pore (5–250 μm) spargers (Parthasarathy and Ahmed, 1996). Because, fine spargers suppressed coalescence and gas-bubble induced turbulence. An increase of sparger number shifts *BSD* to bubbles of small sizes, when the total gas superficial velocity, sparger type and size are constant. *BSD* moves towards larger values as sparger pitch increases (Polli et al., 2002) and turns into a bimodal distribution for a heterogeneous flow (Rabha, 2013). The bimodal distribution combines large and small bubbles (Krishna and Ellenberger, 1996). Besagni et al (Besagni et al., 2016). observed a bimodal *BSD* in the radial direction of BCR in an air-water system up to U_g= 14.9 mm/s. For further increase of U_g= 18.8 mm/s, *BSD* changed from bimodal to unimodal again and the whole distribution curve shifted towards larger bubble sizes. Lau et al (Lau et al., 2016). reported that clustering of bubbles became more apparent as U_g increased from 10.6 to 53.1 mm/s. However, they did not report significant breakup and coalescence of bubbles in BCR.

1.4. *Challenges of image processing and an alternative approach to gas contour quantification*

1.4.1. *Processing of shadowgraph images*

The standard processing steps of shadowgraph images are: optical distortion correction, background subtraction, contrast enhancement, application of filters, thresholding, and determination of the geometrical parameters of a bubble. Due to interaction of bubbles, and high gas flow rate, gas-liquid interface becomes highly fluctuating, and bubbles form cluster. In such cases, processing of bubble images becomes complex. Detecting gas-liquid contour of overlapped bubbles has always been a challenge for the image processing, and there are efforts (Honkanen et al., 2005; Lau et al., 2013; Karn et al., 2015; Zhong et al., 2016; Villegas et al., 2019) to deal with this issue. Proper segmentation (Lau et al., 2013; Villegas et al., 2019), contour verification (Cerqueira et al., 2018) of overlapped bubbles, and resolving blurred images (Poletaev et al., 2020) were so far among the main focuses of these efforts. The discrepancy of result increases with gas flow rate. The scope of image processing algorithm should be expanded, because identifying intersection points, and reconstructing gas-liquid interfaces of merged bubbles are not the only challenges, sometimes bubbles are out-of-focused, and fully overlapped by a cluster of bubbles as well.

1.4.2. *Gas contour quantification based on light intensity*

A camera sensor detects, and produces photoelectrons from the reflected light rays which hit the surface of a bubble. Fig. 2 shows that light rays pass through a gas bubble and some of the rays reflect on the gas-liquid interface. A sensor includes a number of pixels arranged in an array and each pixel has a photodetector. The image, we record is basically the distribution of grayscale value of pixels of a sensor. The profile of gray value indicates the gas contours in a flow domain. Therefore, the probability and the radial distribution of gray values of each pixel ($\varphi(x, y)$) provide a qualitative measure of gas contour distribution and compactness of gas

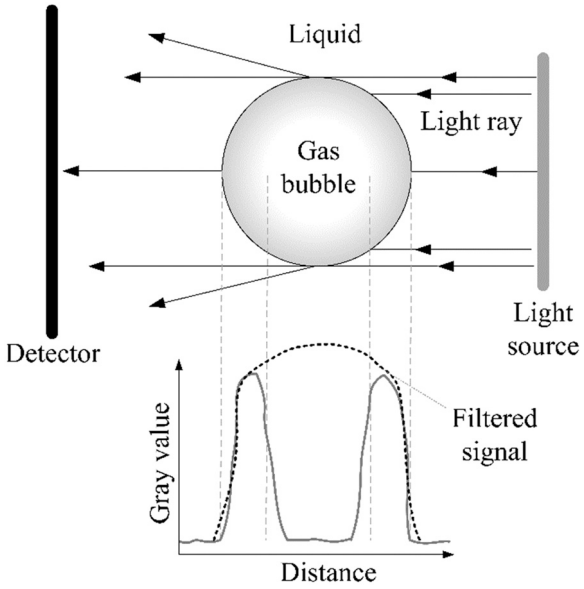

Fig. 2 – Schematic of shadowgraph technique and light intensity profile.

contours at different locations of BCR, respectively. Identifying individual gas fractions from an image is not required according to this approach. Gray value distribution at the radial direction of BCR can be considered as a signal that includes waves. The waves of Fig. 2 are the result of gas-liquid interfaces and a wavelength represents size of gas structure. Therefore, signal analysis approaches can be used to investigate size and repeatability of gas structures.

The power spectral density (*PSD*) and 2D cross-correlation are widely used functions in signal processing, can be employed to analyze bubbly flow. Power spectrum estimates the distribution of signal power among frequencies. *PSD* filters the significant energy by averaging the squared values of a signal, i.e., $\int_{-L}^{L} |I(x, y)|^2 dx$. *PSD* of radial light intensity profile of BCR represents gas structures as a function of its size. The similarity of the gas structure pattern is quantified by using cross-correlation function (*xcorr*). *xcorr* coheres between two different signals and determine the correlation value as a function of time and space. A general expression of *xcorr* is as follows:

$$xcorr(x, y, t) = \langle I_n(x, y, t) I_n(x + \Delta x, y + \Delta y, t + \Delta t) \rangle$$

The above literature review clearly summarizes that a lack of clear knowledge on the dynamics of dissolving bubbles in the dense bubbly flow exists. Moreover, characterizing gas fraction and flow structure by pixel value distribution is possible. On the contrary, this approach is yet widely reported in open literature. A trailblazing experimental technique will help to determine the effect of dissolution of CO_2 bubbles on the hydrodynamics of bubbly flow. Hence, in the present study, we perform experiment to qualitatively characterize the gas fraction distribution, contours, and structures of N_2 and CO_2 gas bubbles in water.

2. Materials and methods

2.1. *Experiments*

The experiments were conducted in a transparent pseudo-2D bubble column (990 mm × 243 mm x 40 mm) which is

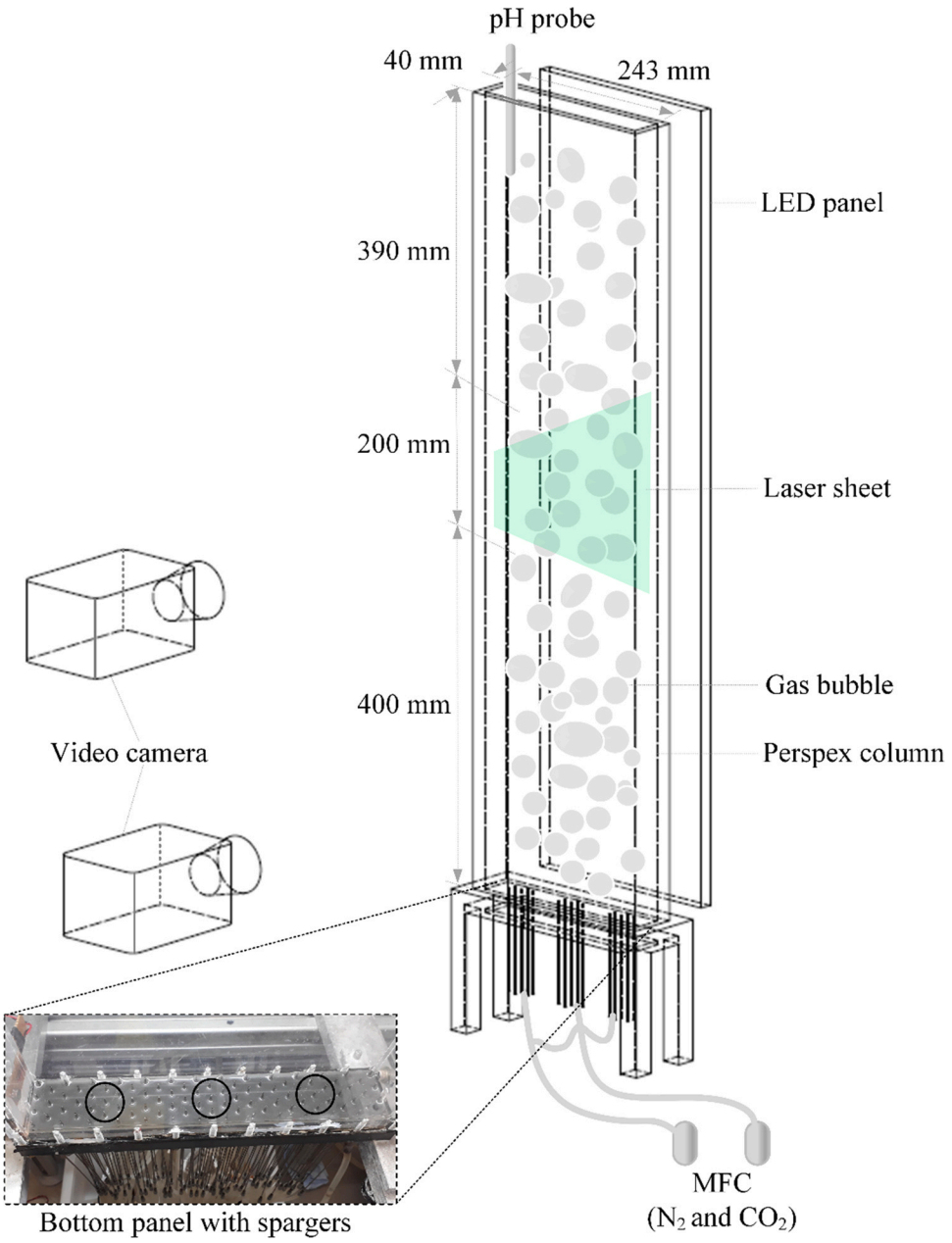

Fig. 3 – Schematic diagram of the test section and the measurement techniques.

made of polymethyl methacrylate (PMMA) at atmospheric pressure and room temperature. A schematic diagram of the test section is shown in Fig. 3. N_2 and CO_2 gas bubbles were injected to the quiescent deionized water of the column using needle spargers. Solubility and density of CO_2 gas in water are almost 90 (Kaye and Laby, 1986) and 1.575 (Hecht et al., 2015) times greater than that of N_2 gas, respectively. Due to a large extent of dissolution characteristics of CO_2 bubbles, DI water becomes acidic (pH range ~7 to ~3.5). Thus, the injection of N_2 and CO_2 gas plumes in water helps us to investigate the effects of mass transfer and hydrodynamics in the bubbly flows. At this point, it is also to be noted that the surface potentials of N_2 and dissolved CO_2 gas bubbles become different as a product of reaction with the bulk liquid. These characteristics of N_2 and CO_2 gas may also have an additional effect on the hydrodynamics of the bubbly flow.

The static water height of the column was maintained at 760 mm. As a result, aspect ratio (AR) became more than 3 and we could neglect the effect of it on the flow regime transition. Needles were fixed at the bottom panel of the column as shown in Fig. 3. The inner diameter of each of the needle and the distance between the consecutive needles were 0.8 mm (fine sparger (Besagni et al., 2018a)) and 10.4 mm, respectively. The needles were patterned with triangular arrays. We have divided 21 needles in 3 groups and each group contains 7 needles. Thus, 3 gas plumes were injected in the column. Two Bronkhorst® mass flow controllers (MFC) (max. flow rate: 20 ln/min) were connected to the needle spargers using flexible tube and valves. One of the MFCs was dedicated to control the flow of CO_2 gas only and another one was for N_2 gas only. The MFCs were calibrated for their respective gases. The software FlowDDE and FlowView operated the flow controllers. The MFCs, tubing and valves were arranged such a way that all the three groups of spargers at a time could inject either N_2 or CO_2 gas. We could also inject N_2 and CO_2 gases respectively through the outer two needle groups and the inner group. The gas injection

Table 1 – Experimental matrix.

Nos.	Gas	U_g (mm/s)	Nos.	Gas	U_g (mm/s)
1	N_2	8.67 ± 0.035	7	CO_2	5.25 ± 1e-4
2		10.70 ± 0.17	8		10.49 ± 1e-4
3		15.11 ± 0.076	9		15.75 ± 0.05
4		20.91 ± 0.075	10		20.99 ± 0.09
5		26.13 ± 0.61	11		26.24 ± 0.9
6		31.62 ± 0.13			

Table 2 – Specifications of optical techniques.

Parameters	Settings
Camera	Imager pro HS 4 M (2016 ×2016 pixels)
Objective	AF Nikkor 28 mm and AF Nikkor 50 mm
Laser	LDY304 PIV series
	Pulse energy: 2 × 30 mJ
	Repetition rate: 0.2–20 kHz
	Optical power: 2×30W

pattern was also possible to alter in our experiment. As a result, our sparger arrangement allows us to investigate dissolving (CO_2) or non-dissolving (N_2) gas driven flow physics. Additionally, mutual effect of dissolving and non-dissolving gas on the flow regime can be studied too. Before performing the experiments, we ensured that all the needles are properly active at a very low superficial gas velocity (approx. 5 mm/s). Each of the experimental conditions were repeated minimum 3 times. Table 1 shows the experiment matrix.

The water becomes acidic due to the dissolution of CO_2 bubbles and a pH probe (InPro 3250i SG/120, Mettler Toledo) measured the pH values of water. The probe was inserted to the column from the top. A few grains of *NaCl* was added to the bulk DI water and that gave a stable pH measurement. We designed the measurement techniques to record bubble image, gas and liquid velocity using so-called optical shadowgraphy, and particle image velocimetry (PIV) techniques. Table 2 summarizes the specifications of visual imaging techniques. We used two high-speed video camera with a LED panel (Fig. 3). One high-speed video camera was employed to capture the bubbles of the whole column (1824 ×1700 pixels) and another one recorded the bubbles at the sparger region (672 ×2016 pixels). The spatial resolutions of the top and the bottom camera were 0.42 ± 0.019 mm/pixel and 0.144 ± 0.004 mm/pixel. A calibration plate was used to find-out the pixel to length ratio. The top camera captured shadowgraph and PIV images at the total recording rate of 1500 Hz. A strobe controller along with the PIV data processing software (DaVis 10.0.5) enabled dynamic control of LED panel and laser light sheet (Fig. 4) such a way that when bubble images were illuminated by LED, laser did not illuminate fluoresecent particles and vice-versa. As a result, the image recording rate of each technique became 750 Hz. The strobe controller also ensured the flicker-free background illumination and the illumination became uniform by using a diffuser on the LED panel. The environmental light did not affect the shadowgraph images as the camera exposure time was short and the experiments were performed in a dark room.

Shadowgraph and PIV imaging techniques were employed to obtain 100 frames for each technique while injecting N_2 gas bubbles with the repetition rate of 750 Hz. Then, the recording was paused and started to record again after 10 s which is called as recording cycle here. In case of CO_2 gas injection, 50 bubble images and 50 PIV images were captured at the same recording speed in a cycle period. Measurement was continued for 2 mins (12 cycles) and 6 mins (36 cycles) respectively for N_2 and CO_2 gas injection. 6 mins recording of CO_2 gas bubbles were sufficient because by that period, *pH* value of water reached to the asymptotic level. Since N_2 gas does not dissolve in water, the recording period was less. The circular and triangular crossed out symbols with dashed lines of Fig. 5 present the *pH* curves for U_g of 5.25 mm/s and 15.75 mm/s, respectively. CO_2 saturates water faster at high $U_g$than that at low U_g. Circular, triangular, and rectangular open symbols of Fig. 5 denote U_g of CO_2 and N_2. The cameras started to record images a few seconds prior to CO_2 gas injection to BCR which was done by LabVIEW. When CO_2 gas was injected to BCR, flow of N_2 gas had been stopped and after 6 mins, CO_2 gas injection was stopped and N_2 gas injection was started. The 'valve steering mode' of MFC was adjusted to achieve the set mass flow rate in short period of time. A quite steady state measurement of mass flow rates was obtained and reduced the uncertainties related to the superficial gas velocities.

2.2. *Image and data processing*

Local gas volume fraction (α_g) distribution was quantified in this study instead of BSD. Because, $\alpha_g$includes both the size and the shape of a gas particle. α_g distribution and radial light intensity profiles of a bubble column are qualitatively compared here. The image and data processing steps for obtaining GVF are explained in this section.

2.2.1. *Processing of shadowgraph images*

Different geometrical parameters of a bubble such as bubble diameter, bubble projection area, bubble shape descriptor and position of a bubble were calculated by processing the raw images. An open-source image processing tool ImageJ had been used to run the image processing operations, identify the contour of a gas fraction and calculate the bubble geometrical parameters. A raw image contains static and dynamic non-uniformities which originate from the illumination of imaging technique, the fluctuation of bubble interface and the environmental light. Additionally, an image may contain traces of unrequired static objects for image processing. We performed following three operations to

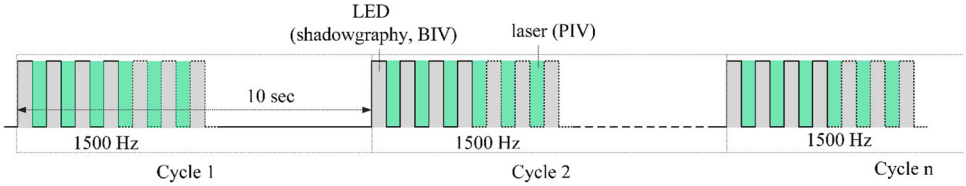

Fig. 4 – Timing of illumination.

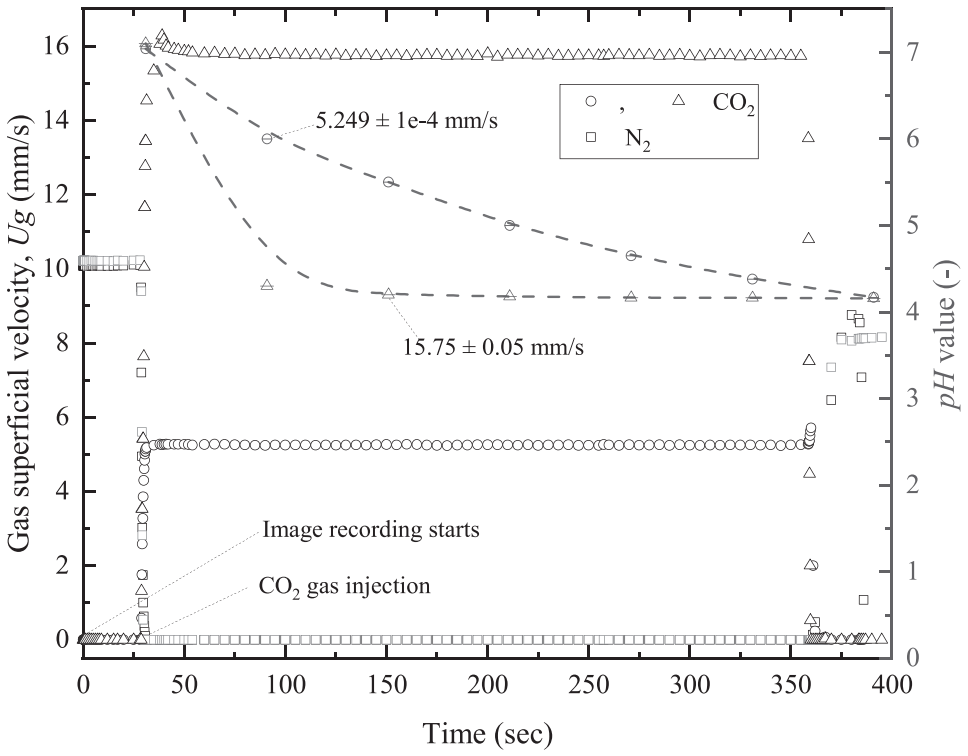

Fig. 5 – Synchronization of mass flow controllers during CO_2 gas injection.

remove all these non-uniformities: background subtraction, light intensity correction, and smoothing. A snapshot of a BCR without bubbles was recorded and subtracted from the raw images. Thus, the experimental uncertainty due to difference in refractive index between water and Perspex glass was minimized. The Gaussian kernel smoothed the raw images. The useful gray value range of an image was set by limiting the minimum and the maximum threshold values from the histogram of the gray values. We found that the threshold limits of an image with CO_2 bubble plumes changed over time. Therefore, a dynamic smoothing-thresholding approach was adopted in the image processing algorithm based on the averaged gray value ($I_{n,th}$) of each image. The thresholding criterion was set depending on the mean gray value of the first image ($I_{1,th}$) of each cycle and applied to the rest of the frames of that cycle. Table 3 shows thresholding and smoothing conditions.

A light ray reflects on the gas-liquid interface and passes through the middle portion of a bubble (Fig. 2). As a result, a hole is noticed in a bubble image which needs to be filled. The built-in filling holes algorithm of ImageJ filled the inner contour of a gas-liquid interface. A proper segmentation of the gas fraction is important for identifying the individual bubbles from clustered and overlapped bubbles. Adjustable Watershed plugin of ImageJ was employed to segment bubbles. The large gas fractions are of highly irregular shape. A common practice to handle such gas fractions is to fit a bubble with an ellipse. Fig. 6(a, b) compares the effect of segmentation and interface fitting filters in terms of average gas count. The averaged gas count vs. local gas volume fraction distribution for a U_g (Fig. 6b) shows that the contour fitting filters do not influence α_g distribution but the results for segmentation vary with U_g. Authors of this article prefer to use the combination of overlay masking and segmentation at high superficial gas velocity, because apparently this combination tracks well the contour of a raw image in detail than the other combinations (Fig. 6a).

Table 3 – Criteria for dynamic smoothing-thresholding.

	Thresholding method	Standard deviation of Gaussian kernel
$I_{n,th} > I_{1,th}$	Shanbhag (Shanbhag, 1994)	σ = 0.40
$I_{n,th} < I_{1,th}$	Otsu (Otsu, 1979)	σ = 0.50

The algorithm for treating the overlapping bubbles mostly addresses the partially overlapped bubbles and not the fully overlapped bubbles. Bubbles are often blurry when they are not in the focal plane and they cannot be processed properly. We ensemble averaged all the frames of a cycle and thus took into account the out-of-focus and the overlapped bubbles. Still the challenges of segmentation and properly tracking the interface sustain. One of the solutions could be to directly analyze the light intensity value distribution of the noise free bubble images which has been followed in this study.

2.2.2. *Data Processing*

Bubble projection area, diameters of minimum bounding rectangle area, major and minor axes of a fitted ellipse, Feret's diameters, shape descriptors (circularity, aspect ratio, solidity) of a gas fraction are directly obtained from ImageJ. Here, solidity and aspect ratio are the ratio of area to convex area and major to minor axis. Circularity value is 1 for a perfect circle and Feret's diameter is the longest distance between any two points along the selection boundary. We distinguish particles of three different shapes: spherical, ellipsoidal and undefined shape based on the values of shape descriptors. Local gas volume fraction ($\alpha_g = V_g/V_{gl}$) is composed of volume of gas fraction, V_g and total local volume of liquid and gas fraction, V_{gl} (Fig. 7). $V_{gl} = F_h.F_v.$ *column depth*, where F_h and F_v are the horizontal and the vertical Feret's diameters. Table 4 summarizes the formulae for calculating

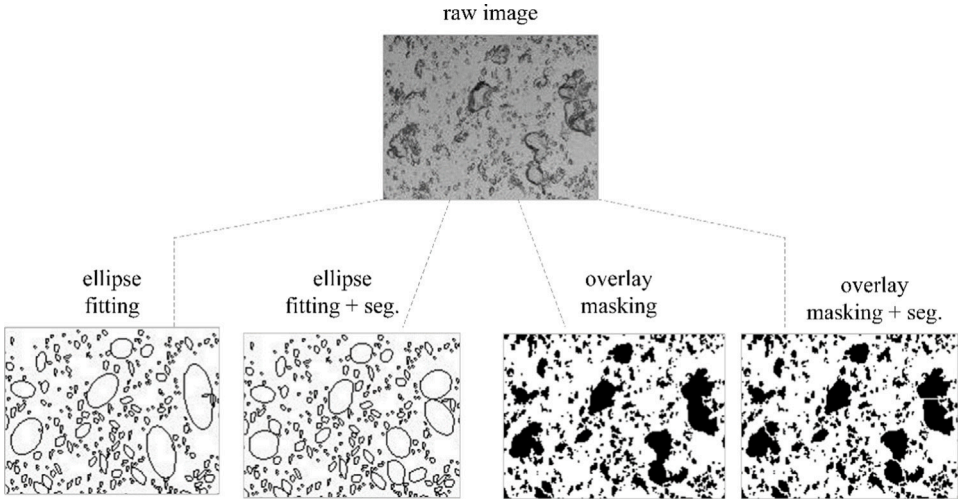

(a)

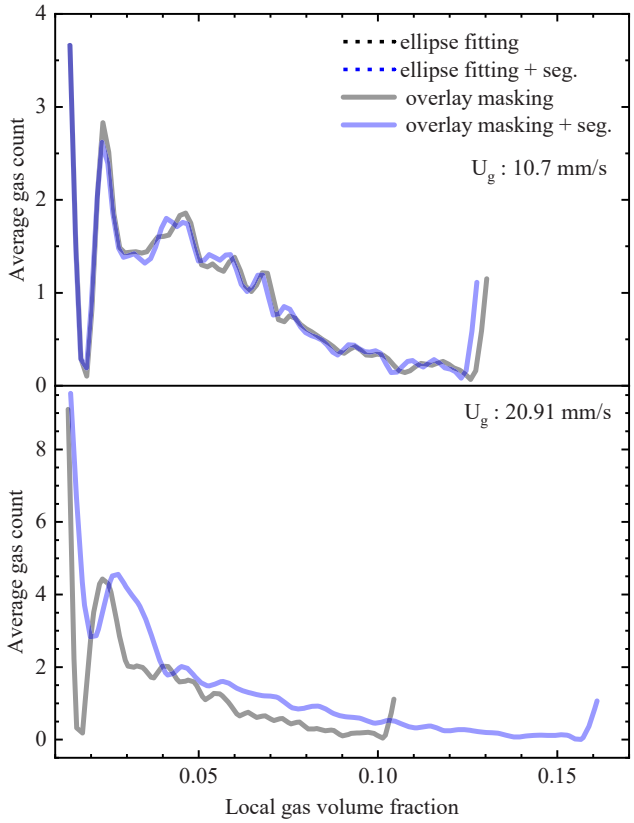

(b)

Fig. 6 – Comparison of gas fraction shape fitting and segmentation by processed images (a), and local gas volume fraction (b).

α_g and the associated conditions. r_x and r_y of spherical and ellipsoidal gas fractions are derived from the minimum bounding rectangle and fit ellipse methods, respectively. The equivalent diameter of the undefined shaped gas fractions is calculated by the concept of equal projection area. MATLAB scripts were written to process further the results of ImageJ and compute local gas volume fraction. Light intensity distribution, power spectrum and cross-correlation value of gas structures were computed as well using MATLAB scripts.

2.3. *Uncertainties*

The sources of measurement uncertainty of optical imaging are non-uniformity of the illumination, distortion due to the environmental effects, constraints of the optics and inadequacy of the image processing algorithms. We have discussed earlier that several attempts were taken to minimize noise and external effects in imaging. The comparison

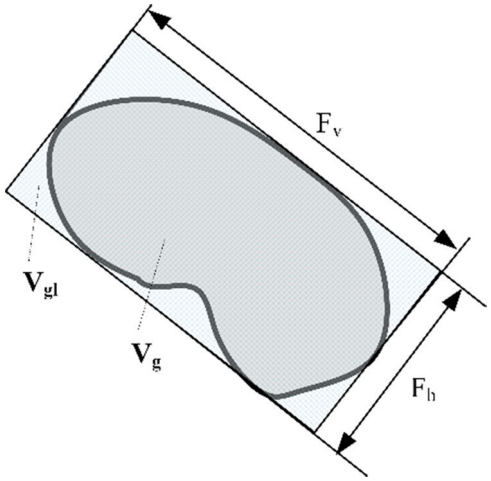

Fig. 7 – Calculation of the local gas volume fraction.

between raw and processed image with the overlay masking method manifests the accurate capture of shape and size of gas particles (Fig. 6a). Thus, the reliability of image processing algorithms was verified. We computed the average deviation between a final processed image and an image with uniform background from their pixel value profiles. The total uncertainty of the bubble images was found ± 0.429 mm. Thus, the measurement errors of shadowgraph imaging are quantified. The *pH* probe was calibrated by following the three-point calibration method of Mettler Toledo software in regular basis. Standard buffer solution of *pH* 4.01, *pH* 7.00 and *pH* 10.01 ensure the reliability of *pH* measurement.

3. Results and discussion

3.1. Gas volume fraction

Local gas volume fractions (α_g) are calculated from geometrical parameters of a bubble (see sub-Section 2.2). We were able to capture evolution of gas fraction distribution at a high frame rate 750 Hz such as $\Delta t = 1.333$ msec for N_2 and CO_2 gas injection to BCR. The results of first 50 frames of each cycle period (0.0667 s) were ensemble averaged. Thus, all the gas fractions of a bubble column are taken into account in the calculation of gas volume fraction. The recordings of bubble images with the high repetition rate mitigates the typical limitations of image processing of bubble cluster and overlapped bubbles.

Superficial gas velocity (U_g) and location of gas fraction have a significant impact on α_g distribution. We divided BCR into multiple rectangular windows (80 ×80 mm^2) to extract the effect of location on α_g distribution. Height of BCR is divided into multiple segments, i.e., from 680 mm to 760 mm (A), from 440 mm to 520 mm (B) and from 200 mm to 280 mm (C). In the lateral direction, the bubble column is split from 77 mm to 152 mm (M) and from 152 mm to 228 mm (NW). A, B, C, M and NW are the name of segments. Thus, we show the results of top-middle (A-M), middle-middle (B-M), bottom-middle (C-M), top-right (A-NW), middle-right (B-NW), and bottom-right (C-NW) regions of BCR for different U_g. The temporal evolution of ensemble averaged PDF and radial density of α_g for different U_g of N_2 and CO_2 bubble plumes are elucidated in this section using Figs. 8 and 9.

3.1.1. Probability distribution function of α_g

The PDFs of N_2 gas volume fraction infer that α_g between 0.03 and 0.075 is in large number and distribution of α_g is unimodal at U_g= 8.67 mm/s (Fig. 8a). The distribution becomes bimodal and small α_g (0.01–0.03) appears with the increase of U_g. The PDFs shift towards small α_g while U_g changes from 10.7 to 15.7 mm/s. If U_g further increases to 20.91 mm/s, the distribution shifts more towards small α_g and the unimodal distribution tends to appear again. The peaks of bimodal distribution of large α_g at U_g= 10.7 and 15.11 mm/s and the peak of unimodal distribution of U_g= 8.67 mm/s are in the same range of α_g (~ 0.045). The first peaks (e.g., α_g) of bimodal distribution could be the result of bubble-bubble interaction at high U_g. The distribution of α_g is generally independent of time for N_2 gas, whereas CO_2 gas bubbles show a dependency with time especially at U_g= 5.25 and 10.49 mm/s (Fig. 9a). The dependency is strong in first 3 mins of the recording period, then it decreases gradually. The probability of small α_g has been found higher at window A than that window C in first 4 mins. It infers that CO_2 bubbles dissolve in water while rising. At high U_g (15.75–26.24 mm/s), CO_2 gas bubbles saturate the bulk DI water in a short period of time. As a result, the effect of CO_2 bubble dissolution on the temporal evolution of α_g is not clearly visible. But we can see that the local α_g of CO_2 bubbles are relatively smaller in comparison to N_2 bubble plumes at high U_g and bimodal distributions are not vividly visible (e.g., at U_g= 15.75 mm/s). It reflects that the outcomes of the bubble-bubble interaction of N_2 and CO_2 bubbly flows are different.

Due to bubble plume wandering, relatively smaller gas fractions are found in large number near the wall of a BCR than that in the middle of a column for both N_2 and CO_2 bubbles. All the PDFs of N_2 and CO_2 bubble plumes clearly exhibit this phenomenon, except for CO_2 gas plumes at the lowest (5.25 mm/s) and the highest (26.24 mm/s) U_g. The plume oscillation is weak at the lowest U_g= 5.25 mm/s and consequently, the behavior of gas fraction distribution in the horizontal direction alters. At the highest U_g (26.24 mm/s), all sizes of α_g mix up in the column and distinction of small and large gas fractions at the particular locations of a BCR is not clearly visible.

3.1.2. Radial distribution function of α_g

Radial distribution function (RDF) determines the probability of finding the particle center and measure the compactness or the density of particles in a defined region. ImageJ calculates the weighted average of brightness of x and y coordinates of all the pixels of a gas fraction. We used these averaged coordinate values to identify the position of a gas fraction and calculated the radial distribution function using the following expression:

$$g(r) = \frac{\int_r^{r+dr} \sum_{i=0}^{i=n} n_i}{N.\ 2\pi R}.$$

Where, N is the total number of gas fraction in a window, R is the radial distance of the window and $\sum_{i=0}^{i=n} n_i$ is the summation of gas fractions' number within the particular circular region. The compactness of N_2 and CO_2 bubbles in the different locations of a column with U_g has been discussed here.

Fig. 8b shows that compactness of N_2 and CO_2 bubbles of all the windows gradually increases as the radial distance of a window increases. $g(r)$ generally, becomes maximum within 30–45 mm and decreases after that. The compactness of α_g is proportionally correlated with the column height for

Table 4 – Equation to calculate the bubble size and gas fraction.

Shape	Formula	Condition
Spherical	$D_{eq,sp} = 2.(r_x^2.r_y)^{1/3}$. $V_{g,sp} = \frac{4}{3}\pi(0.5.D_{eq,sp})^2$.	AR < 1.50, *circularity* > 0.75 and *solidity* ≥ 0.8.
Ellipsoidal	$V_{g,ellip} = \frac{4}{3}\pi(r_x.r_y.r_z)$.where r_z=r_x.	AR ≥ 1.50, AR ≤ 2.00 and *solidity* ≥ 0.8.
Undefined	$D_{eq,un} = 2\sqrt{\frac{A_{proj}}{\pi}}$. $V_{g,un} = \frac{4}{3}\pi(0.5.D_{eq,un})^2$.	*solidity* ≤ 0.8.

N_2 bubbles. It justifies that a rising N_2 bubble plume diffuses outward and the axial oscillation of a rising plume reduces. Small bubbles become less dynamic at the upper part of the column. Contrary to N_2 bubble plumes, the compactness of CO_2 bubbles are higher at the bottom part of a bubble column than that at the upper part of a column (Fig. 9b). Since CO_2 bubbles dissolve while rising and N_2 bubbles do not, such difference is quite obvious. Dissolved CO_2 bubbles are small and they can easily be entrapped by a recirculating flow. Gas fractions are more in number within 30–40 mm at window C-NW compared to window A-NW at same radial distance. Recirculation zones are created near the bubble column wall and because of that $g(r)$ for both N_2 and CO_2 bubbles increase from the middle to the side of a column. Therefore, PDFs and RDFs of gas volume fraction resemble that the availability of dense small bubble increases near the wall and at the upper part of a bubble column. Radial distribution of α_g does not show a significant dependency on time. For example, an irregular distribution of void fraction with respect to time is clear at 40.2 mm of the near wall windows for CO_2 bubbly flows.

3.1.3. *Flow structures in dense bubbly flow*

Local gas structures of dissolving (e.g., CO_2) and non-dissolving (e.g., N_2) bubbles in dense bubbly flow are discussed with the snapshots of the raw videos (Fig. 10). $\acute{B}$ and $\acute{D}$ are at the middle and at the bottom of BCR. The temporal evolutions of local α_g of CO_2 gas bubbles confirm that bulk DI water is adequately saturated by CO_2 at 360 s (Fig. 9a). Thus, the snapshots of CO_2 bubbles at 1 s and 360 s respectively represent flows before and after the saturation. The features of Fig. 10 a and b are as follows:

i) The flow structures due to CO_2 gas bubbles change over time significantly and in case of N_2 gas bubbles, flow structures do not alter.
ii) Both N_2 and CO_2 bubbly flows become dense with the increase of U_g.
iii) Large gas fractions are not available in N_2 bubbly flow for U_g of 26.128 mm/s.
iv) Size of CO_2 bubbles are more homogeneous than that of N_2 bubbles for both saturated and unsaturated bulk water.
v) CO_2 bubbly flows produce many small bubbles after being saturated.
vi) α_g distribution at the sparger region for CO_2 gas bubbles is quite different than that for N_2 gas bubbles for U_g up to 21 mm/s (approx.).
vii) CO_2 bubbles are reluctant to be coalesced and large gas fractions are not noticed at U_g of 15.75 mm/s and

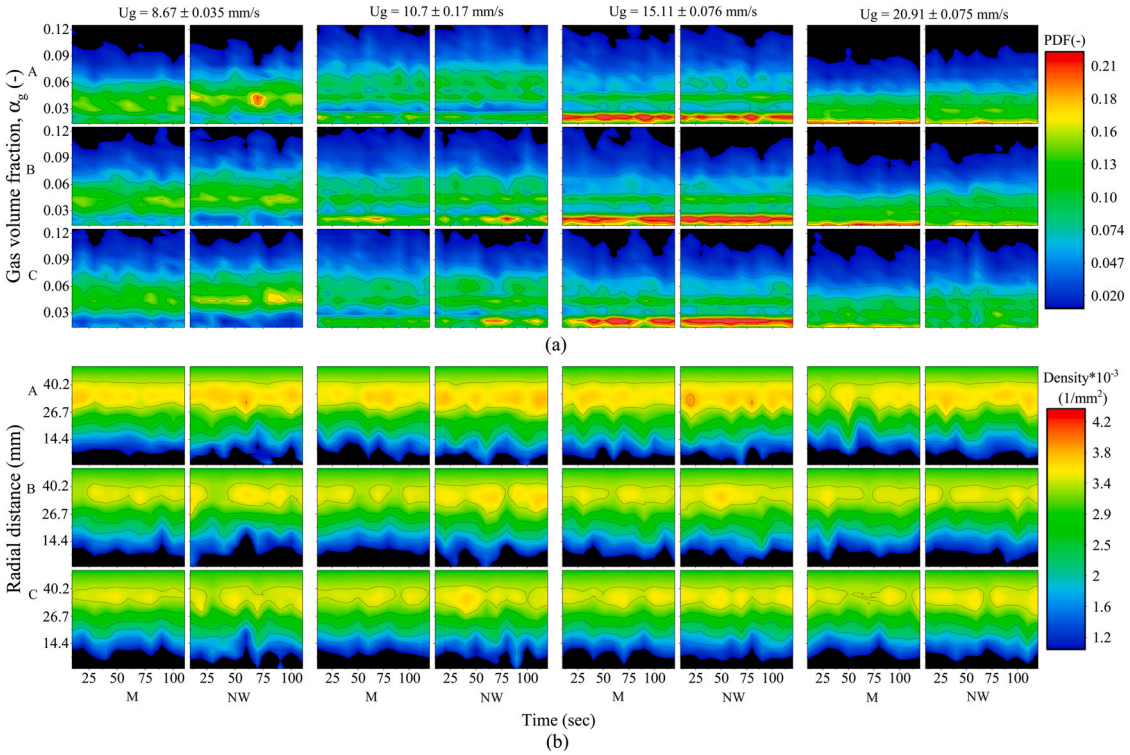

Fig. 8 – Normalized probability (a) and radial distribution (b) of local gas fraction of N_2 plumes.

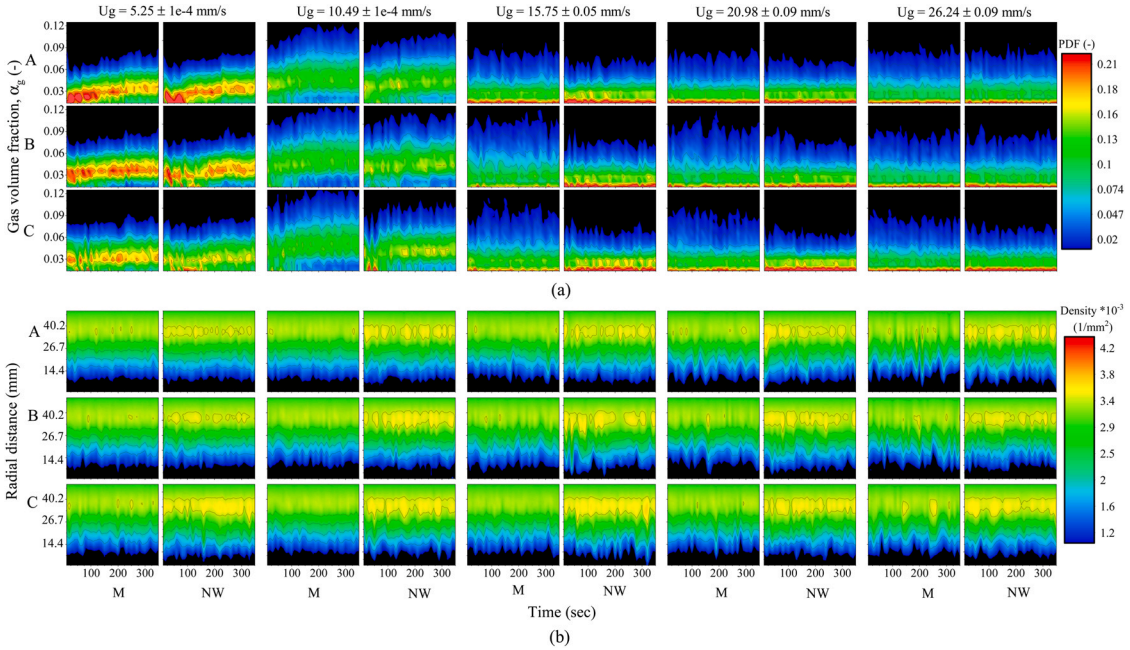

Fig. 9 – Normalized probability (a) and radial distribution (b) of local gas fraction of CO_2 plumes.

20.99 mm/s. At a very high U_g= 26.24 mm/s, bubble rising velocity is high and resistance in bubble coalescence may not sufficient. Hence, large gas fraction may come into sight which disappears in saturated CO_2 bubbly flow.

CO_2 gas produces many small bubbles at the sparger region. Small bubbles inhibit coalescence as they suppress turbulence. Another reason of hindering CO_2 bubble coalescence is hypothesized in the sub-Section 1.4. pH value of flow with CO_2 bubbly flow decreased to a plateau. It means that CO_2 bubbles do not dissolve in water anymore and size of CO_2 bubbles supposedly remain constant. Therefore, one might deduce that CO_2 bubbly flow after being saturated may act like a N_2 bubbly flow. But, α_g distribution of CO_2 bubbly flow (at 360 s) is quite different than N_2 bubbly flow. Hence, it can be argued that the geometrical size of a gas fraction alone is not sufficient enough to characterize a flow phenomenon, rather the fluid properties and interface dynamics should be taken into account as well.

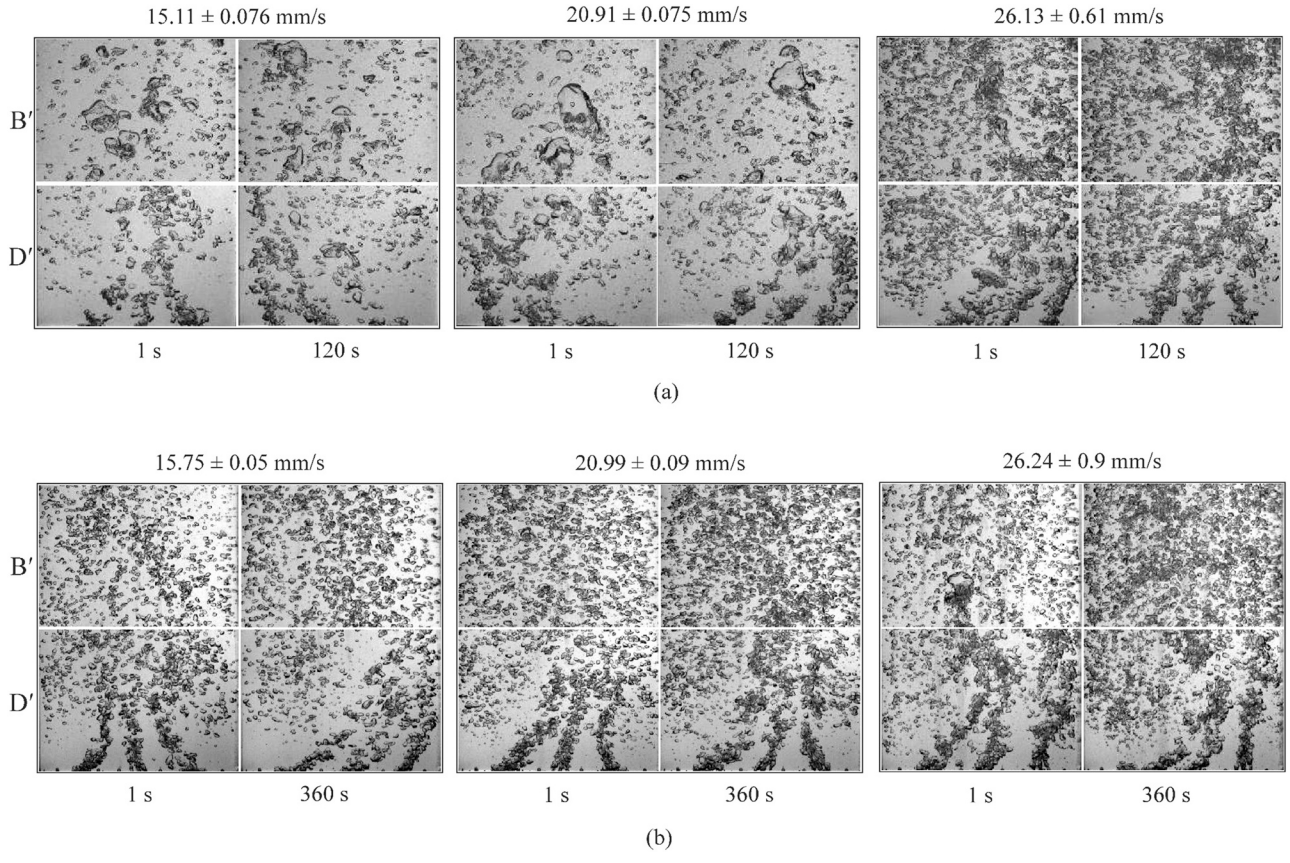

Fig. 10 – Snapshots of bubble images at different superficial gas velocities in (a) N_2 and (b) CO_2 bubbly flow (non-scaled).

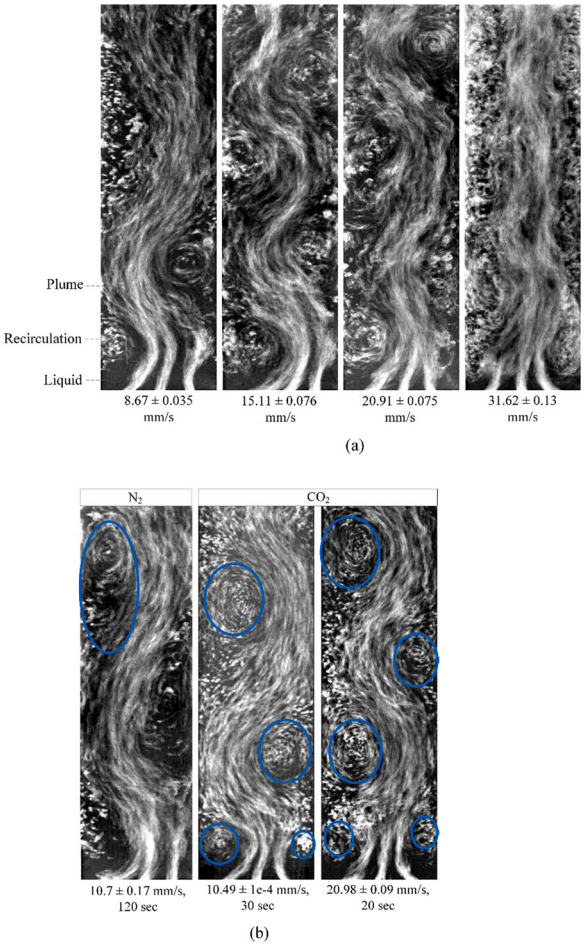

Fig. 11 – Effect of N_2 superficial gas velocities (a) and CO_2 gas dissolution (b) on the flow structures.

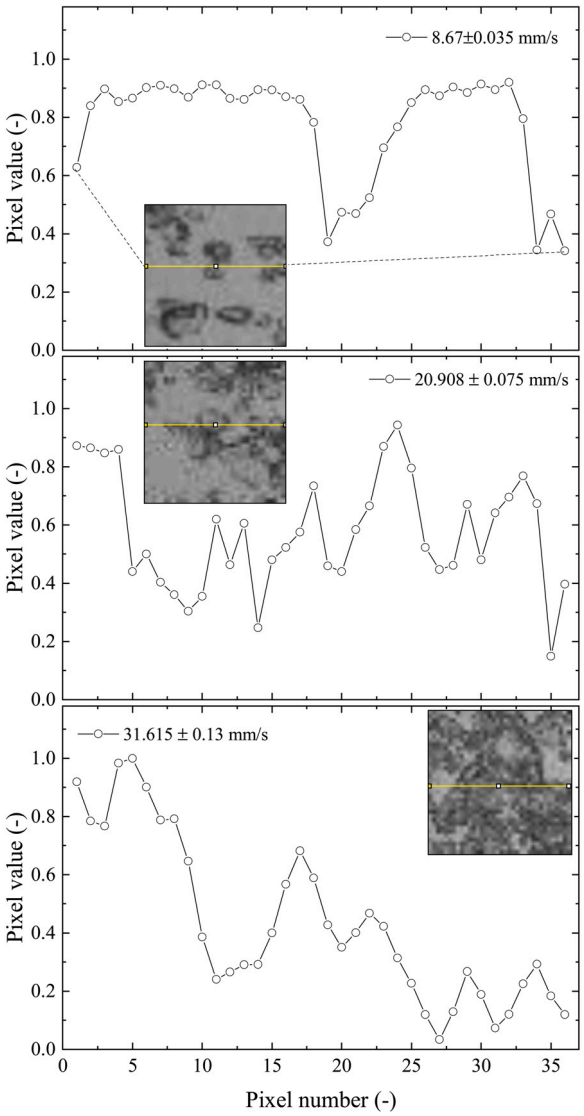

Fig. 12 – Radial light intensity profile in the middle of a bubble column at different gas superficial velocities of N_2 plume.

Oscillating bubble plumes were investigated several authors (Delnoij et al., 1997; Mudde and Simonin, 1999). In this study, intensity pixel values over a sequence of frames of a recording cycle have been averaged to study the behavior of wandering plume (Fig. 11). A plume oscillates both in the axial and the radial directions in a 2D BCR. The oscillating plumes does not touch the column wall just after the gas injection at 8.67–10.7 mm/s since transverse velocity of these bubbles is very low. At intermediate U_g(15.11 – 20.91 mm/s), plumes at the sparger region oscillate as well and reach to the side walls of BCR. In case of high U_g= 20.91–31.62 mm/s, a gas plume does not oscillate much and rises through the middle part of BCR and the small recirculating zones appear near the side walls of it. The number of recirculating zones increases and their sizes decrease especially at the upper part of the bubble column while U_g increases from 8.67 mm/s to 15.11 mm/s (Fig. 11a). Due to further increasing of U_g, a plume becomes unsteady and the shape of recirculating zone appears. The vortical structure in the upper left region of the column moves downward and consequently, pushes the plume downward. It leads to generate small recirculating zones. Dissolution of CO_2 bubbles results to an increasing number of recirculating zones and decreasing of vortex size. Fig. 11b clarifies that plume oscillation frequency increases, as U_g of CO_2 gas increases from 10.49 to 20.98 mm/s.

3.2. *Light intensity*

Each pixel of a gray-level image has a value correspond to the intensity of light at that particular point. The light intensity or pixel values of a grayscale image has been analyzed to characterize the contours of gas fractions. Because, a few steps of image processing recipe such as segmentation, identification of the gas-liquid interface become challenging at high U_g and by adopting the technique which used pixel values to determine gas contour, we can overcome the above-mentioned limitations of common image processing methods. Thereby, investigation of gas fraction distribution for high superficial gas velocity (e.g., U_g > 25 mm/s) and disordered gas bubbles at the gas-sparger region are also in the scope of this technique. The gas bubble contour and liquid of a raw image resemble dark (=0) and bright color (=1). Low and high intensity values thus respectively represent gas and liquid (Fig. 12). As bubbly flow becomes dilute to dense, gas fraction increases with the gas-liquid interface that leads to decrease of the average pixel intensity value of an image.

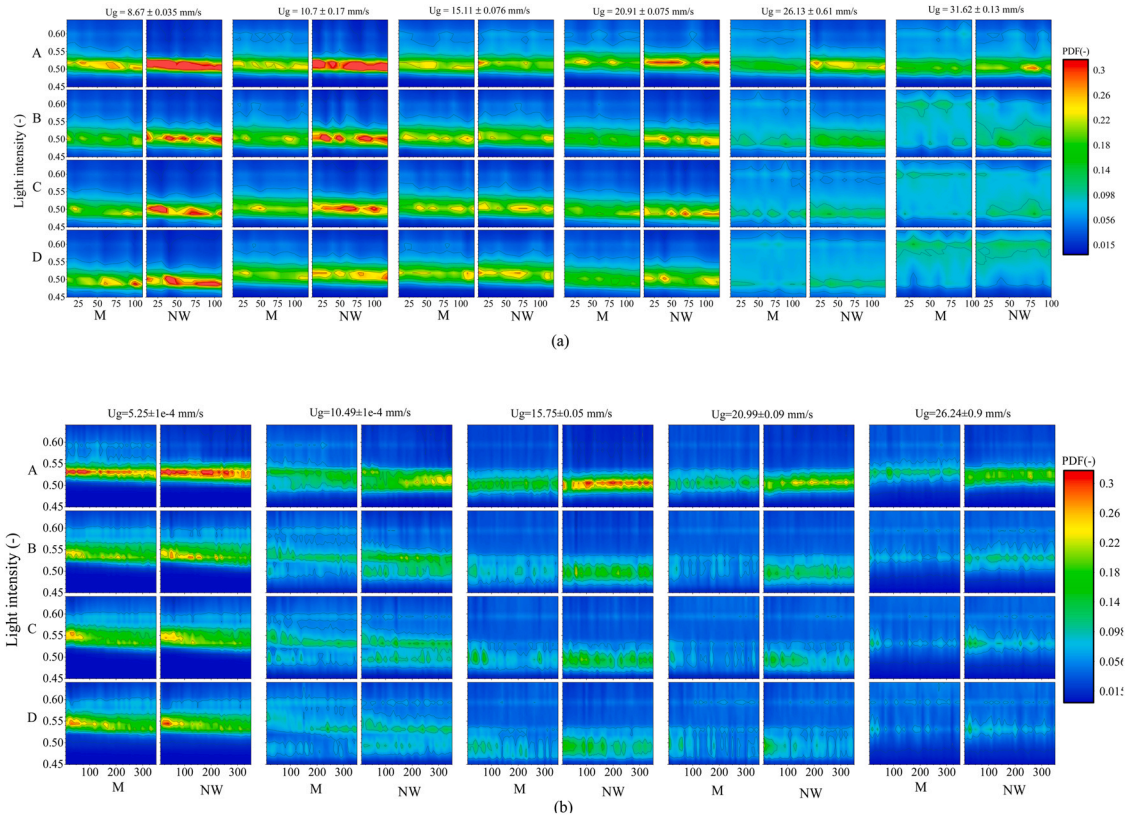

Fig. 13 – Normalized probability distribution of the light intensity values of each pixel for N_2 (a) and CO_2 (b) gas plumes.

Fig. 12 clearly demonstrates that a negative correlation exists between the number of pixel values and the gas fractions in dense bubbly flow. In case of a highly dynamic gas-liquid interface, light rays scatter and reflect in an irregular pattern. As a result, the reflected light rays on an irregular gas-liquid interface consist of a wide range of pixel values. Light rays do not deflect much after reflecting on a quasi-static gas-liquid interface. Therefore, a narrow distribution of low pixel values is obtained at low U_g that indicates a flow as a homogeneous bubbly flow.

Fig. 13 shows the effect of U_g on the pixel intensity distribution at 8 different locations of a bubble column reactor with N_2 and CO_2 bubble plumes. The position of first 6 locations were defined in the sub-Section 2.1. There is an additional axial division in BCR from 1 mm to 80 mm, which is denoted as '*D*' in Fig. 13. Light intensity distribution curves show that pixel values are normally distributed and peaks of distribution curve repeat themselves with non-periodic motion. A distribution curve widens and the deviation of PDFs increases with the increasing U_g (Fig. 13 a and b). The availability of bright light tremendously increases at U_g= 26.13 mm/s and 31.62 mm/s (Fig. 13 a). As mentioned earlier, presence of bright light does not resemble only liquid but also scattering light due to fluctuating gas-liquid interfaces, is an outcome of non-uniform oscillating gas-liquid interfaces in a dense or heterogenous bubbly flow. It confirms that a homogeneous bubbly flow regime becomes heterogeneous as U_g increases. Fig. 13 a and b show that availability of a particular range of gray value (0.48–0.53) is higher at top-right regions (A-NW, B-NW) of BCR than that at bottom-middle regions (C-M, D-M). Because, bubbles in the recirculating zones which are near BCR wall causes less scattering of light. The comparison between gray distribution at the middle of BCR than that at near the wall clarifies that differences in PDFs diminish in the radial direction of BCR with the increase of U_g. From these facts, it can be inferred that gas fraction near the wall and upper part of BCR are less dynamic and uniformly distributed. Additionally, the flow becomes highly dynamic and heterogeneous due to high U_g. Since intensity value distribution does not directly quantify bubble sizes, we did not notice unimodal or bimodal distribution of gas fraction.

Fig. 13 b shows that the width of pixel value distribution changes with time. The dynamic features of these PDFs relate the dissolution characteristics of CO_2 bubbles for U_g of 5.249 mm/s and 10.49 mm/s (Fig. 13 b). A bubbly flow is saturated by dissolved fraction of CO_2 bubbles include small (dissolved) and large (non-dissolved) bubbles since the dissolubility of CO_2 bubbles gradually diminish. PDFs of CO_2 bubbly flow at U_g= 10.49–20.99 mm/s expand in both the directions, is an indication of different size of bubbles. Liquid and highly dynamic gas fraction both are the source of low light intensity value. It might be considered as one of the limitations of this approach. As well as the peak points of the light intensity PDFs are influenced by U_g and time. Moreover, the homogeneity of the illumination of shadowgraph, optics etc. affect the intensity of pixel value and contribute in shifting the PDFs. Therefore, fixing a common gas or liquid representative pixel value is quite challenging. In spite of all these challenges, analyzing light intensity distribution is useful to qualitatively characterize the different flow regimes.

3.3. *Power spectral density*

Power spectral density (PSD) has been employed to estimate the dominant gas structure size in BCR. A horizontal light intensity profile at a particular height of BCR with uniform background is considered as a signal. A profile of pixel values of a bubbly flow has a number of waves. The shape,

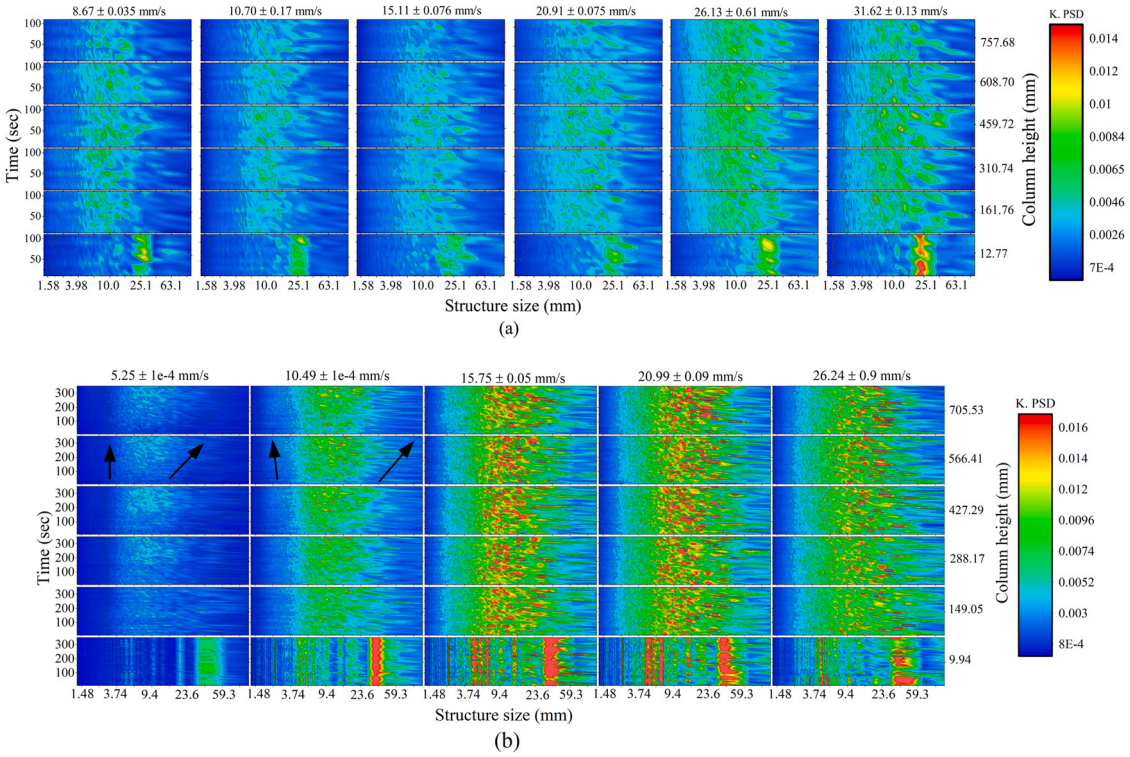

Fig. 14 – Normalized power spectral density of N_2 (a) and CO_2 (b) gas plumes for different superficial gas velocities.

wavelength and number of waves of a signal depend on the radial gas fraction distribution. A bubble cluster or overlapped bubbles result a complex signal. A PSD of pixel value profile identifies the gas fractions within the signal and their corresponding spatial extents. PSDs are multiplied by the corresponding frequencies to compute the real spectrums. Fig. 14 a and b present the power spectrum of N_2 and CO_2 bubbly flow at several heights of BCR for different U_g.

The bottom part (< 15 mm) of both N_2 and CO_2 bubbly flow show that the gas structure sizes are ~30 mm, where the diameter of a group of spargers is 21.6 mm. The size of each individual plume at the bottom part of the column should be a bit larger than the injectors' diameter which is close to the determined gas structure size (~ 30 mm). The dominant gas structure of our experiments is ~ 10 mm. The gas fraction size varies in between 4 mm and 25 mm for N_2 bubbly flow at low U_g (< 15.11 mm/s). The large gas structures (25 mm) in the middle of the column height (459.72 mm) at U_g= 8.67 mm/s - 15.11 mm/s confirm that N_2 bubbles merge in this region of BCR and form large clusters even at low U_g. The span of dominant gas structures expands for U_g of 20.91 mm/s – 31.62 mm/s (Fig. 14 a). A wide span of gas fractions includes small and large gas fractions which are produced due to breakup and coalescence.

Fig. 14 b shows that the temporal evolution of PSD of CO_2 bubbly flow is different than that of N_2 bubbly flow which is evident at U_g= 5.25 mm/s and 10.49 mm/s. A negative correlation between gas structure and time is visible in the middle of BCR. The small gas fraction (4 mm) does not decrease with time, because dissolution of bubble reaches to the asymptotic level. These bubbles may be considered as the remaining of the dissolved bubbles. Left arrows in Fig. 14 b at column height of 566.41 mm depict the dissolved bubbles. Inclined arrows pointing upward indicates the increasing trend of gas fraction with time. As dissolution continues, gas fractions are found to be increased from 9.4 mm to 30 mm in BCR. The wavelength of pixel intensity profile becomes highly non-uniform at high U_g because of bubble cluster, overlapped bubbles etc. Therefore, PSDs of heterogeneous CO_2 bubbly flow consist of a wide range of gas structure size all over the bubble column.

3.4. *2D Cross-correlation*

Cross-correlation function identifies the similarity of two patterns relative to each other. This section focuses on computing the cross-correlation of 2D patterns of gas structures. One of the patterns can be named as a reference pattern and another one is a target pattern. The reference pattern is correlated with a sequence of target patterns as a function of time and space. When the two patterns are exactly the same, the correlation value is 1. The correlation value decreases as the deviation between reference and target pattern increases and at one point, the value reaches to the asymptotic level.

Sub-Section 2.1 mentioned that we recorded total 12 cycles of N_2 bubbly flow and 36 cycles of CO_2 bubbly flow. To avoid a major part of the dissolution effect of CO_2 bubbles on time-correlation, we have analyzed last 20 cycles of it. Each cycle is considered as individual realization for time-domain cross-correlation calculation. The whole bubble column is sliced in multiple windows (42.3 ×45.1 mm²). The middle frame (25th) of each cycle of a window is assumed as a reference window and correlated with the corresponding upstream and downstream windows. The correlation values of these two streams are found symmetric with respect to the reference window. Hence, it would be sufficient to analyse one side of the symmetry. As there is no distinguishable effect of bubble column height on the cross-correlation, normalized cross-correlation values as a function of time difference (ΔT) and U_g are shown in Fig. 15a and b. For a particular U_g, multiple curves with dots are plotted for different windows in the vertical direction of a column.

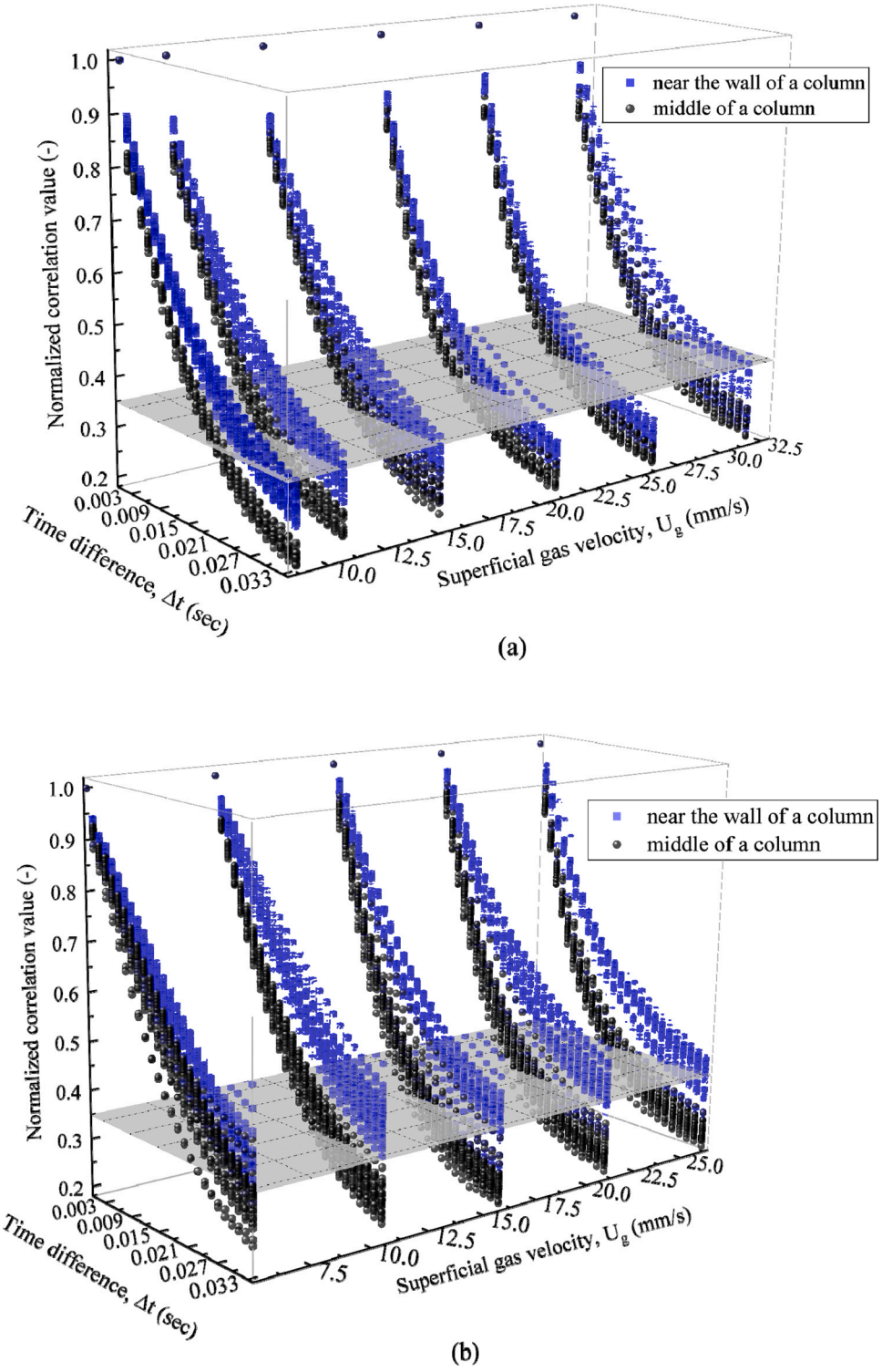

Fig. 15 – 2D Cross-correlation as a function of time for N_2 (a) and CO_2 (b) gas plumes.

Clusters of N_2 and CO_2 gas fraction lose their structure faster in the middle of BCR than those near the column wall. Between N_2 and CO_2 bubbly flows, gas structures of N_2 are more dynamic and the effect of column height is less pronounced for all U_g. Fig. 15a shows that time requires for a gas structure near the wall losing its pattern is inversely proportional to U_g till 20.99 mm/s and then, it is positively correlated. The reason is that gas distribution is highly dense for U_g of 26.13 mm/s and 31.62 mm/s. Compact gas structures do not change over time. But for a high U_g= 31.62 mm/s, effect of column height on the dynamics of gas structure can slightly be noticed. The gas structures of N_2 bubbly flow tremendously change and become highly dense for U_g of 26.13 mm/s and 31.62 mm/s. This might retard the loss of cross-correlation at high U_g. The correlation values diverge at the highest U_g= 31.62 mm/s. Unlike N_2 gas fractions, the correlation values of CO_2 do not show a non-linear relationship with U_g and gas structures are quite dissimilar along the column height (Fig. 15b).

4. Conclusions

In the present study, we have experimentally investigated dilute to dense bubbly flow in a quasi- 2D bubble column with N_2 and CO_2 gas bubbles in deionized water. The solubility of CO_2 gas in water is much higher than that of N_2. An optical shadowgraph technique of high spatial and temporal resolution recorded the bubble images. The standard image processing steps were followed to process the bubble images which pose challenges on segmentation of bubble cluster and overlapped bubbles. An alternative approach based on the pixel values was employed and qualitatively analysed the bubbly flow phenomena for a range of superficial gas velocities of 5–30 mm/s (approximately). The functions of signal analysis power spectral density and cross-correlation characterized the gas structures.

Relatively large gas fractions are produced in N_2 bubbly flows with the increase of superficial gas velocities and further increase of superficial gas velocity breaks the large gas fraction into small pieces. CO_2 bubbles are found to dissolve in water. But they are reluctant to coalesce during dissolution. This behaviour does not disappear even when water is saturated by CO_2 bubbles. The plausible reason for this is that carbonaceous species around a bubble result positive surface charge and energy barrier. This energy barrier hinders the coalescence of CO_2 bubbles. Small gas fractions at the sparger region also possibly inhibit CO_2 bubble coalescence and this phenomenon results difference in gas fraction distribution in comparison with that of N_2 bubbles. The future work may focus on exploring gas and liquid velocity profiles and gas injection pattern to justify the dynamic behaviour of gas structures.

Declaration of Competing Interest

The authors declare that they have no known competing financial interests or personal relationships that could have appeared to influence the work reported in this paper.

Acknowledgement

The authors gratefully acknowledge the Netherlands Organisation for Scientific Research (NWO) for the financial support of this study.

References

Heijnen, J.J., Van'T Riet, K., 1984. Mass transfer, mixing and heat transfer phenomena in low viscosity bubble column reactors. Chem. Eng. **28**.
Panicker, N.S., 2017. Computational Models for Turbulent Bubbly Flows in Bubble Columns, in. Mechanical Engineering. Iowa State University.
Kantarci, N., Borak, F., Ulgen, O.K., 2005. Bubble column reactors. Process Biochem. 40 (7), 2263–2283.
Besagni, G., Inzoli, F., Ziegenhein, T., 2018a. Two-Phase Bubble Columns: A Comprehensive Review. ChemEngineering 2 (2) 13-13.
Laupsien, D., 2017. Hydrodynamics, mass transfer and mixing induced by bubble plumes in viscous fluids, in Laboratoire d'Ingénierie des Systèmes Biologiques et des Procédés (LISBP). Inst. Natl. Des. Sci. Appliquées (INSA) De. Toulouse.
Mudde, R.F., Harteveld, W.K., Van, H.E.A., 2009. Den Akker. Unif. Flow. Bubble Columns 148–158.
Besagni, G., Gallazzini, L., Inzoli, F., 2018b. Effect of gas sparger design on bubble column hydrodynamics using pure and binary liquid phases. Chem. Eng. Sci. 176, 116–126.
Schaefer, R., Merten, C., Eigenberger, G., 2002. Bubble size distributions in a bubble column reactor under industrial conditions. Exp. Therm. Fluid Sci. 26, 595–604.
Wilkinson, P.M., L.L.L, 1990. Pressure and gas density effects on bubble break-up and gas hold-up in bubble columns. Chem. Eng. Sci. 45 (8), 2309–2315.
Krishna, R., Wilkinson, P.M., Van Dierendonck, L.L., 1991. A model for gas holdup in bubble columns incorporating the influence of gas density on flow regime transitions. Chem. Eng. Sci. 46 (10), 2491–2496.
Hecht, K., Bey, O., Ettmüller, J., Graefen, P., Friehmelt, R., Nilles, M., 2015. Effect of gas density on gas holdup in bubble columns. Chem. -Ing. -Tech. 87 (6), 762–772.
Risso, F., 2018. Agitation, mixing, and transfers induced by bubbles. Annu. Rev. Fluid Mech. 50, 25–48.
Ruzicka, M.C., et al., 2001. Homog. – Heterog. Regime Transit. Bubble Columns 56, 4609–4626.
Mudde, R.F., 2005. Gravity-driven bubbly flows. Annu. Rev. Fluid Mech. 37, 393–423.
Zahradník, J., Fialová, M., Růžička, M., Drahŏs, J., Kaštánek, F., Thomas, N.H., 1997. Duality of the gas-liquid flow regimes in bubble column reactors. Chem. Eng. Sci. 52 (21–22), 3811–3826.
Darmana, D., N.G. Deen, R.L.B.H., Kuipers, J.A.K., 2007. Detailed modelling of hydrodynamics, mass transfer and chemical reactions in a bubble column using a discrete bubble model: Chemisorption of CO_2 into NaOH solution, numerical and experimental study. Chem. Eng. Sci. 62, 2556–2575.
Hlawitschka, M.W., P.K, K.Z.ähringer, H.-J, Bar, 2017. Simulation and experimental validation of reactive bubble column reactors. Chem. Eng. Sci. 170, 306–319.
Colombet, D., Dominique, L., Risso, F., Cockx, A., Guiraud, P., 2015. Dynamics and mass transfer of rising bubbles in a homogenous swarm at large gas volume fraction. J. Fluid Mech. 763, 254–285.
Weiner, A., C. Pesci, J.T., Grewe, J., Hoffmann, M., Schlüter, M., Bothe, D., 2019. Experimental and numerical investigation of reactive species transport around a small rising bubble. Chem. Eng. Sci. 1, 1–18.
Aboulhasanzadeh, B., Tryggvason, G., 2014. Effect of bubble interactions on mass transfer in bubbly flow. Int. J. Heat. Mass Transf. 79, 390–396.
Nock, W.J., Heaven, S., Banks, C.J., 2016. Mass transfer and gas-liquid interface properties of single CO_2 bubbles rising in tap water. Chem. Eng. Sci. 140, 171–178.
Farajzadeh, R., Barati, A., Delil, H.A., Bruining, J., Zitha, P.L.J., 2007. Mass transfer of CO_2 into water and surfactant solutions. Journal of Petroleum Science and Technology. 25, 1493–1511.
Kong, G., 2019. Hydrodynamics and mass transfer in bubbly flow: an experimental study. Eindh. Univ. Technol.
Li, X., P. Zhang, W.W., G. Chen, J.Li, 2019a. Interactions between gas–liquid mass transfer and bubble behaviours. Royal Society Open. R. Soc. Open Sci. 6, 190136.
Huang, J., Saito, T., 2015. Influence of bubble-surface contaminationon instantaneous mass transfer. Chem. Eng. Technol. 38, 1947–1954.
Harper, J.F., 2007. Bubble rise in a liquid with a surfactant gas, in particular carbon dioxide. J. Fluid Mech. 581, 157–165.
Yaminsky, V.V., Ohnishi, S., Vogler, E.A., Horn, R.G., 2010. Stability of aqueous films between bubbles. Part 1. The effect of speed on bubble coalescence in purified water and simple electrolyte solutions. Langmuir 26, 8061–8074.
Tabor, R.F., Chan, D.Y.C., Grieser, F., Dagastine, R.R., 2011. Anomalous stability of carbon dioxide in pH-controlled bubble coalescence. Angew. Chem. Int. Ed. 50, 3454–3456.
Tabor, R.F., Greiser, F., Dagastine, R.R., Chan, D.Y.C., 2012. Measurement and analysis of forces in bubble and droplet systems using AFM. J. Colloid Interface Sci. 371, 1–14.
Katsir, Y., Marmur, A., 2014. Rate of bubble coalescence following quasi-static approach: Screening and neutralization of the electric double layer. Sci. Rep. 4, 1–7.
Lucas, D., Ziegenhein, T., 2019. Influence of the bubble size distribution on the bubble column flow regime. Int. J. Multiph. Flow. 120, 1–11.
Marrucci, G., Nicodemo, L., 1967. Coalescence of gas bubbles in aqueous solutions of inorganic electrolytes. Chem. Eng. Sci. 22, 1257–1265.
Polli, M., Stanislao, M.D., Bagatin, R., Bakr, E.A., Masi, M., 2002. Bubble size distribution in the sparger region of bubble columns. Chem. Eng. Sci. 57 (1), 197–205.

Rabha, S., Schubert, M., Wagner, M., Lucas, D., Hampel, U., 2013. Bubble size and radial gas hold-up distributions in a slurry bubble column using ultrafast electron beam x-ray tomography. Am. Inst. Chem. Eng. 59, 1709–1722.
Krishna, R., Ellenberger, J., 1996. Gas holdup in bubble column reactors operating in the churn-turbulent flow regime. Am. Inst. Chem. Eng. 42, 2627–2634.
Besagni, G., et al., 2016. Estimation of bubble size distributions and shapes in two-phase bubble column using image analysis and optical probes. Flow. Meas. Instrum. 52 (July), 190–207.
Lau, Y.M., S. Azizi, K.M., Schubert, M., 2016. Voronoï analysis of bubbly flows via ultrafast X-ray tomographic imaging. Exp. Fluids 57, 1–12.
Honkanen, M., Saarenrinne, P., Stoor, T., Niinimäki, J., 2005. Recognition of highly overlapping ellipse-like bubble images. Meas. Sci. Technol. 16, 1760–1770.
Lau, Y.M., Deen, N.G., Kuipers, J.A.M., 2013. Development of an image measurement technique for size distribution in dense bubbly flows. Chem. Eng. Sci. 94, 20–29.
Karn, A., Ellis, C., Arndt, R., Hong, J., 2015. An integrative image measurement technique for dense bubbly fl ows with a wide size distribution. Chem. Eng. Sci. 122, 240–249.
Zhong, S., Zou, X., Zhang, Z., Tian, H., 2016. A flexible image analysis method for measuring bubble parameters. Chem. Eng. Sci. 141, 143–153.
Villegas, L.R., Colombet, D., Guiraud, P., Legendre, D., Cazin, S., Cockx, A., 2019. Image processing for the experimental investigation of dense dispersed flows: application to bubbly flows. Int. J. Multiph. Flow. 111, 16–30.
Cerqueira, R.F.L., Paladino, E.E., Ynumaru, B.K., Maliska, C.R., 2018. Image processing techniques for the measurement of two-phase bubbly pipe flows using particle image and tracking velocimetry (PIV / PTV). Chem. Eng. Sci. 189, 1–23.
Parthasarathy, R., Ahmed, N., 1996. Size distribution of bubbles generated by fine-pore spargers. J. Chem. Eng. Jpn. 29, 1030–1034.
Poletaev, I., Tokarev, M.P., Pervunin, K.S., 2020. Bubble patterns recognition using neural networks: Application to the analysis of a two-phase bubbly jet. Int. J. Multiph. Flow. **126**.
Kaye, G.W.C., Laby, T.H., 1986. Tables of Physical and Chemical Constants. Longman, pp. 1.
Shanbhag, A.G., 1994. Utilization of information measure as a means of image thresholding. CVGIP: Graph. Models Image Process. 56 (5), 414–419.
Otsu, N., 1979. A threshold selection method from gray-Level histograms. IEEE Trans. Syst., Man, Cybern. 9 (1), 62–66.
Delnoij, E., J.A.M.K, van Swaaij, W.P.P., 1997. Dynamic simulation of gas-liquid two-phase flow: effect of column aspect ratio on the flow structure. Chem. Eng. Sci. 52, 3759–3772.
Mudde, R.F., Simonin, O., 1999. Two- and three-dimensional simulations of a bubble plume using a two-fluid model. Chem. Eng. Sci. 54, 5061–5069.
Weiner, A., Bothe, D., 2017. Advanced subgrid-scale modeling for convection-dominated species transport at fluid interfaces with application to mass transfer from rising bubbles. J. Comput. Phys. 347, 261–289.
Li, J., Cheng, Y., Chen, X., Zheng, S., 2019b. Impact of electroviscous effect on viscosity in developing highly concentrated protein formations: Lessons from non-protein charged colloids. Int. J. Pharma. X 1, 1–9.
Harteveld, W., 2005. Bubble columns: Structures or stability? Ph. D. Thesis, Technische Universiteit Delft, The Netherlands.